It has been a challenge for turbulence computations to capture the geometrical complexities of real-life applications such as cars and airplanes. Geometry is a major driver of complexity in these problems, as it selects the morphology and energetics of coherent structures sustaining the turbulence. As an example of the LBM's capabilities, in Fig. 3 we plot streamlines of flow past a realistic car geometry, with various window offsets as well as wheels and wheel houses. This simulation locates the major morphological structures of the flow. The detail-tracking capabilities of LBM are best appreciated by inspecting the pressure distribution at the center line around this car shape (see Fig. 4). The computed drag is typically within 5% of experiment.

LBM's Cartesian mesh proves instrumental to the task of automating and accelerating the grid generation process, and the control of physical realizability in the Boltzmann representation is highly robust, avoiding the need for difficult and time-consuming manual code and geometry adjustments. Other details of the PowerFLOW code, including the formulation of boundary conditions, are given in (*32*). Once the CAD specification is provided for the flow geometry, grid generation requires several orders of magnitude less time than with conventional methods based on the Navier-Stokes equations, whereas the run times of the turbulence simulations themselves may be an order of magnitude faster. Also, once the functional form of τ_{turb} in Eq. 4 is prescribed, there is no adjustment of parameters in the basic code or in the turbulence model. This strategy has been carefully tested and compared with experiments for a wide variety of car geometries (*36, 37*).

References and Notes

1. L. Boltzmann, *Sitzungber. Kais. Akad. Wiss. Wien Math. Naturwiss. Classe* **66**, 275 (1872).
2. C. Cercignani, *Theory and Application of the Boltzmann Equation* (Elsevier, New York, 1975).
3. S. Chapman, T. Cowling, *The Mathematical Theory of Non-Uniform Gases* (Cambridge Univ. Press, Cambridge, 1952).
4. L. Landau, E. Lifshitz, *Fluid Mechanics* (Pergamon, Oxford, 1987).
5. U. Frisch, *Turbulence, The Legacy of A. Kolmogorov* (Cambridge Univ. Press, Cambridge, 1996).
6. U. Frisch, S. Orszag, *Phys. Today* **43**, 24 (1990).
7. K. R. Sreenivasan, *Rev. Mod. Phys.* **71**, S383 (1999).
8. A. Kolmogorov, *Dokl. Akad. Nauk. SSSR* **30**, 9 (1941).
9. J. Boussinesq, *C. R. Acad. Sci. Paris* **71**, 389 (1870).
10. B. Launder, D. Spalding, *Comp. Mech. Appl. Mech. Eng.* **3**, 269 (1974).
11. V. Yakhot, S. Orszag, *J. Sci. Comput.* **1**, 3 (1986).
12. V. Yakhot, S. Orszag, S. Thangam, T. Gatski, C. Speziale, *Phys. Fluids A* **4**, 1510 (1992).
13. P. Bhatnagar, E. Gross, M. Krook, *Phys. Rev. A* **94**, 511 (1954).
14. G. Wannier, *Statistical Physics* (Dover, New York, 1966).
15. A. V. Bobylev, *Sov. Phys. Dokl.* **27**, 29 (1982).
16. I. V. Karlin, A. N. Gorban, *Ann. Phys.* **11**, 783 (2002).
17. S. Succi, I. Karlin, H. Chen, S. Orszag, *Physica A* **280**, 92 (2000).
18. H. Chen, S. Succi, S. Orszag, *Phys. Rev. E* **59**, R2527 (1999).
19. S. Succi, O. Filippova, H. Chen, S. Orszag, *J. Stat. Phys.* **107**, 261 (2002).
20. S. Ansumali, I. V. Karlin, *Phys. Rev. E* **62**, 7999 (2000).
21. B. M. Boghosian, J. Yepez, P. V. Coveney, A. J. Wagner, *Proc. R. Soc. London Ser. A* **457**, 717 (2001).
22. S. Ansumali, I. V. Karlin, *Phys. Rev. E* **65**, 056312 (2002).
23. S. Succi, I. Karlin, H. Chen, *Rev. Mod. Phys.* **74**, 1203 (2002).
24. O. Pashko, Y. Oono, *Int. J. Mod. Phys. B* **14**, 555 (2000).
25. R. Benzi, S. Succi, M. Vergassola, *Phys. Rep.* **222**, 145 (1992).
26. S. Chen, G. Doolen, *Annu. Rev. Fluid Mech.* **30**, 329 (1998).
27. S. Succi, *The Lattice Boltzmann Equation for Fluid Dynamics and Beyond* (Oxford Univ. Press, Oxford, 2001).
28. G. McNamara, G. Zanetti, *Phys. Rev. Lett.* **61**, 2332 (1988).
29. F. Higuera, S. Succi, R. Benzi, *Europhys. Lett.* **9**, 345 (1989).
30. H. Chen, S. Chen, W. Matthaeus, *Phys. Rev. A* **45**, 5339 (1992).
31. Y. Qian, D. d'Humieres, P. Lallemand, *Europhys. Lett.* **17**, 479 (1992).
32. H. Chen, C. Teixeira, K. Molvig, *Int. J. Mod. Phys. C* **9**, 1281 (1998).
33. See www.exa.com/newsite/frames/powerflowmaster.html.
34. R. Shock *et al.*, *J. Aircraft* **39**, 434 (2002).
35. D. P. Lockard, L. S. Luo, S. D. Milder, B. A. Singer, *J. Stat. Phys.* **107**, 423 (2002).
36. W. Bartelheimer, *SAE Paper 20015332* (2001).
37. R. Lietz, S. Mallick, S. Kandasami, H. Chen, *SAE Paper 20020154* (2002).

38. We thank R. Benzi, B. Boghosian, S. Chen, U. Frisch, J. Hoch, I. Karlin, A. Karpikov, S. Mallick, H. C. Oettinger, Y. Qian, S. Remondi, K. Sreenivasan, I. Staroselsky, R. Zhang, and B. Alder for discussions. Supported by NSF grant DMS9974289.

Supporting Online Material

www.sciencemag.org/cgi/content/full/301/5633/633/DC1

Figs. S1 to S3

28 March 2003; accepted 10 June 2003

Stratospheric Memory and Skill of Extended-Range Weather Forecasts

Mark P. Baldwin,[1] David B. Stephenson,[2] David W. J. Thompson,[3] Timothy J. Dunkerton,[1] Andrew J. Charlton,[2] Alan O'Neill[2]

We use an empirical statistical model to demonstrate significant skill in making extended-range forecasts of the monthly-mean Arctic Oscillation (AO). Forecast skill derives from persistent circulation anomalies in the lowermost stratosphere and is greatest during boreal winter. A comparison to the Southern Hemisphere provides evidence that both the time scale and predictability of the AO depend on the presence of persistent circulation anomalies just above the tropopause. These circulation anomalies most likely affect the troposphere through changes to waves in the upper troposphere, which induce surface pressure changes that correspond to the AO.

Deterministic prediction of daily weather, using numerical forecast models, is limited to several days. As the lead time increases to a week and beyond, deterministic prediction of the weather for a particular day gives way to stochastic prediction of the time-averaged weather, which is more predictable than its instantaneous state (*1*). Weather forecasts beyond 10 days are called "extended-range" predictions (*2*); they may be ensemble forecasts, in which many model forecasts with slightly differing initial conditions are averaged together, or they may be based on empirical statistical models trained on historical data.

Forecast skill in predicting the time-averaged state of the atmosphere beyond 10 days comes in part from slow and predictable influences of Earth's surface. In the Northern Hemisphere extratropics, the main contributor to predictability is tropical sea surface temperature anomalies (*3*, *4*), with possible contributions from soil moisture, vegetation, snow and ice cover, land surface temperature and albedo, and sea ice movement and extent. Forecast skill also derives from memory within the atmosphere, or phenomena with long lifetimes, such as the Madden-Julian Oscillation in the tropical troposphere (*5*). There is growing evidence that additional extended-range tropospheric forecast skill may also come from slow variations of the circulation of the stratosphere (*6–8*).

In general, the largest spatial scales of atmospheric variability are more persistent and easier to forecast than the smaller scales. The Arctic Oscillation (AO) (*9*), similar to the North Atlantic Oscillation (*10*, *11*), is a planetary-scale pattern of near-surface (1000 hPa) variability, characterized by movement of atmospheric mass between high and low latitudes and a corresponding out-of-phase relation, or dipole, in the strength of the zonal (*12*) flow along ~55°N and ~35°N. AO variations are associated with wintertime climate variations throughout the middle- and high-latitude continental regions. These changes include not only

[1]Northwest Research Associates, 14508 NE 20th Street, Bellevue, WA, 98007, USA. [2]Department of Meteorology, University of Reading, Reading RG6 6BB, UK. [3]Department of Atmospheric Science, Colorado State University, Fort Collins, CO 80523, USA.

average conditions but also day-to-day variability, modulating rainfall and storm tracks, the frequency of occurrence of high-latitude blocking events, and cold air outbreaks (*13*).

The Northern Annular Mode (NAM) is identical to the AO at 1000 hPa, but we define it separately at each isobaric level from Earth's surface through the stratosphere (*14*). Time-height analysis of the NAM links variations in the strength of the stratospheric polar vortex downward to the AO (*15*). Stratospheric NAM variations, which are driven mainly by upward-propagating planetary-scale waves of tropospheric origin, tend to descend through the stratosphere and create persistent NAM anomalies just above the tropopause (*7*, *16*). On average, lower stratospheric NAM anomalies are followed by persistent AO anomalies of the same sign (*7*). This observation suggests that the time scale of the NAM may be a key to understanding how stratospheric circulation anomalies affect the troposphere.

We define the time scale of NAM anomalies as the time for the autocorrelation function of the NAM to decrease to $1/e$ ($\sim$0.368, the "*e*-folding time"). On the basis of data from 1958 to 2002 (*17*), we find that the time scale of the NAM in the stratosphere is greater than that in the troposphere during all seasons (Fig. 1A). The time scale of the AO is greatest during winter, which is coincident with the longest NAM time scale in the lowermost stratosphere.

We hypothesize that, during winter, the time scale of the AO is increased by persistent NAM anomalies in the lowermost stratosphere. By itself, the coincidence of the tropospheric and stratospheric maxima (Fig. 1A) is merely suggestive of stratosphere-troposphere coupling. For evidence in support of our hypothesis, we examine the time scale of the Southern Annular Mode (SAM) (*18*). In the troposphere, the time scale of the SAM has a peak during late spring (November and December) superposed on a gentle annual cycle that is maximized during winter (Fig. 1B). The late-spring maximum in the time scale of the tropospheric SAM coincides with the largest SAM anomalies just above the tropopause (Fig. 1C). Climatologically, the Southern Hemisphere stratospheric polar vortex is strong throughout the winter, with relatively small SAM anomalies. It is not until spring, when the vortex begins to diminish, that interaction between the waves and the mean flow results in large SAM anomalies (*19*). The breakdown of the Southern Hemisphere vortex begins in the upper stratosphere and progresses downward. This process is reflected in the time-height development of the SAM variance; the maximum in SAM variance progresses downward during spring, peaking during November and December just above the tropopause. The maximum time scale of the tropospheric SAM (Fig. 1B) aligns precisely with the maximum SAM variance just above the tropopause (Fig. 1B). In both hemispheres, the time scale of the tropospheric annular mode is a maximum when the amplitude of lower stratospheric annular-mode anomalies is largest (*20*). The longer time scale of the AO during winter is also consistent with general circulation model experiments in which the time scale of the AO is found to decrease when stratospheric variability is artificially suppressed (*21*).

The observation that long-lived AO anomalies tend to follow stratospheric NAM anomalies of the same sign suggests the use of a statistical model in which the NAM at one or more levels is used to predict the time-averaged value of the AO (*22*). Data analysis (*23*) suggests that there is a linear relationship between NAM anomalies in the lower stratosphere and subsequent AO anomalies, so that a linear statistical model appears to be an appropriate way to investigate the relationship between stratospheric NAM values and future values of the AO. We demonstrate this technique by predicting the monthly-mean AO, with a forecast period beginning after 10 days in order to exclude the initial time period when numerical forecasts of daily weather have appreciable skill. Our linear prediction model uses the present value of the NAM at one level between 1000 and 10 hPa to

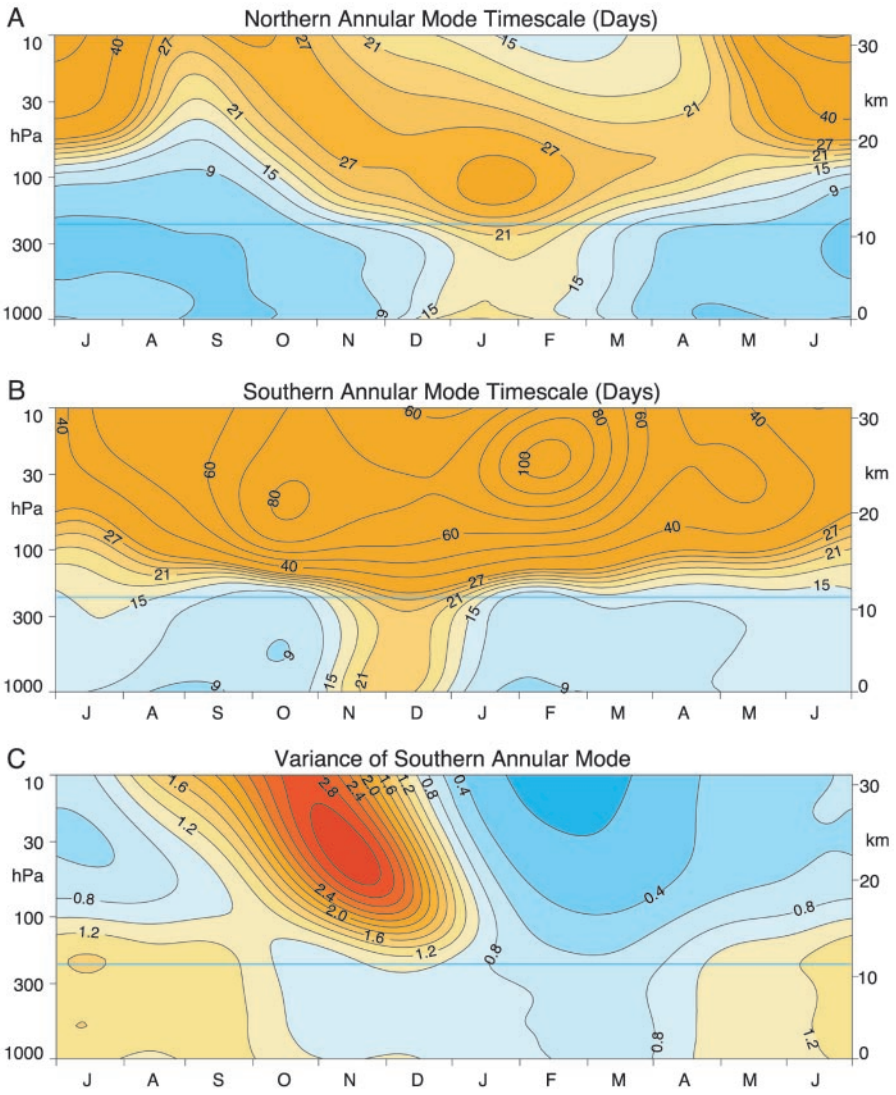

Fig. 1. (**A**) Time scale of the NAM as measured by the time (days) for the autocorrelation function to drop to $1/e$ ($\sim$0.378). The horizontal line in each panel represents the approximate tropopause. Daily values are a time average using Gaussian weighting with a full width at half maximum (FWHM) of 60 days (σ = 26 days). The time scale is estimated with a least-squares fit of an exponential curve to the autocorrelation function. The contour interval is 3 days up to 30 days, and 10 days at higher values. (**B**) The time scale of the SAM, measured as in (A). (**C**) Variance of the SAM. Daily values were obtained with the same methodology as in (A). The SAM time series at each level are normalized to unit standard deviation.

predict the monthly-mean AO beginning 10 days later: $\bar{A}(t + L) = \beta_0 + \beta_1 N(t) + \varepsilon$, where A represents the AO, $L = 10 + (30/2) = 25$ days, $\bar{A}(t + L)$ represents the one-month mean of the AO centered on time $t + L$ (starting at time $t + L - 15$ and continuing to time $t + L + 15$), $N(t)$ represents the NAM at one level at time t, β_0 and β_1 are regression parameters to be estimated, and ε represents noise.

We performed least-squares regressions to calculate the percent variance of $\bar{A}(t + L)$ that is accounted for by the predictor series $N(t)$ (*24*), as a function of height and time of year (Fig. 2A). Predictability of the AO was greatest during the extended winter season (October through April). The stratospheric NAM was a better predictor of the AO than the AO was of itself—and it did so for a longer season (Fig. 2B). The optimum single level for forecasting the AO is 150 hPa (~13 km), which is the lowest data level that lies entirely above the tropopause in the extratropics.

In order to test the predictability of the AO, it is necessary to make forecasts and assess their skill. When we used all years of December through February data, the NAM at 150 hPa accounted for 20.2% of the variance of the AO 10 to 40 days later (*25*). In order to avoid artificial skill (*26*), we performed cross-validated forecasts by removing one winter at a time, estimating β_0 and β_1, and then forecasting the missing winter. The cross-validated skill dropped slightly to 17.9%. If instead of the 150-hPa NAM, the AO was used to predict itself, the cross-validated skill was 12.3%. We also tried forecasts using both the 150-hPa NAM and the AO together, but we obtained an identical cross-validated skill of 17.9%, indicating that the AO adds no information that is not already in the 150-hPa NAM and that the 150-hPa NAM is a sufficient predictor (*27*).

Our prediction methodology uses annular mode indices as both predictors and predictands, so the results thus far have demonstrated only that the forecasting relationship projects onto the annular mode patterns. There is no reason to believe a priori that the annular mode patterns optimize the relationship between circulation anomalies in the lowermost stratosphere and subsequent 1000-hPa anomalies. We used maximum covariance analysis (MCA) (*28*) to pair daily 150-hPa geopotential fields with monthly-mean 1000-hPa fields centered 25 days later. We found that the MCA patterns for 1000 and 150 hPa were nearly identical to the AO and 150-hPa NAM patterns, respectively (Fig. 3). The optimal spatial patterns for both the predictor and predictand were nearly identical to the annular mode patterns.

The interaction between NAM anomalies just above the tropopause (~150 hPa) and waves in the upper troposphere (~300 hPa) may be the primary mechanism by which stratospheric anomalies induce changes to the troposphere (*29*). Both synoptic-scale and planetary-scale waves penetrate the lowermost stratosphere, providing a region of overlap between the NAM anomalies and the waves. Based on the observations (Figs. 1 to 3), we reason that the lower stratospheric NAM (or some similar quantity involving zonal-mean wind) must be involved in coupling to the troposphere.

Previous work has shown that the tropospheric NAM is driven by transient momentum flux anomalies (*30*). These anomalies tend to occur over a broad latitudinal band, peaking in midlatitudes, so that the momentum-flux convergence anomalies form a north-south dipole, forcing both the NAM and a dipole in zonal-mean wind. The response to any such forcing is both a zonal wind acceleration and a mass redistribution (changes to surface pressure) as part of an induced circulation in the meridional plane (*31*). Through this mechanism, upper tropospheric momentum-flux anomalies lead directly to AO changes (*32*).

For specific evidence that lower stratospheric NAM anomalies affect momentum fluxes in the upper troposphere, we examined how the 150-hPa NAM is related to lag correlations between 300-hPa eddy momentum fluxes and the 300-hPa NAM (*33*, *34*). We categorized each day during December through February by whether or not the NAM anomalies increased in magnitude between 300 and 150 hPa. This methodology is nearly equivalent to categorization based on the vertical shear of the zonal-mean wind. On 38% (1575) of the days, the NAM anomaly strengthened with height (i.e., had the same sign anomaly at both levels and was numerically larger at 150 hPa). We compared the distributions of the 300-hPa NAM for the two categories and found that neither the standard deviation nor the mean differed significantly from that for all days (*35*).

When the NAM strengthened with height, upper tropospheric momentum-flux anomalies were more effective at forcing upper tropospheric NAM anomalies of the same sign, and they did so for a longer time (Fig. 4A). When the NAM weakened with height, the lag correlations were smaller and dropped to near zero within a few days. This difference supports the hypothesis that the lower stratospheric NAM modulates momentum fluxes in the upper troposphere.

We find that both planetary-scale waves and synoptic-scale waves are involved. The propagation of planetary waves is particularly sensitive to wind anomalies just above the tropopause (*36*), but planetary waves 1 and 2 account for only ~25% of the variance of the momentum flux at 300 hPa. When the NAM strengthened with height, momentum fluxes

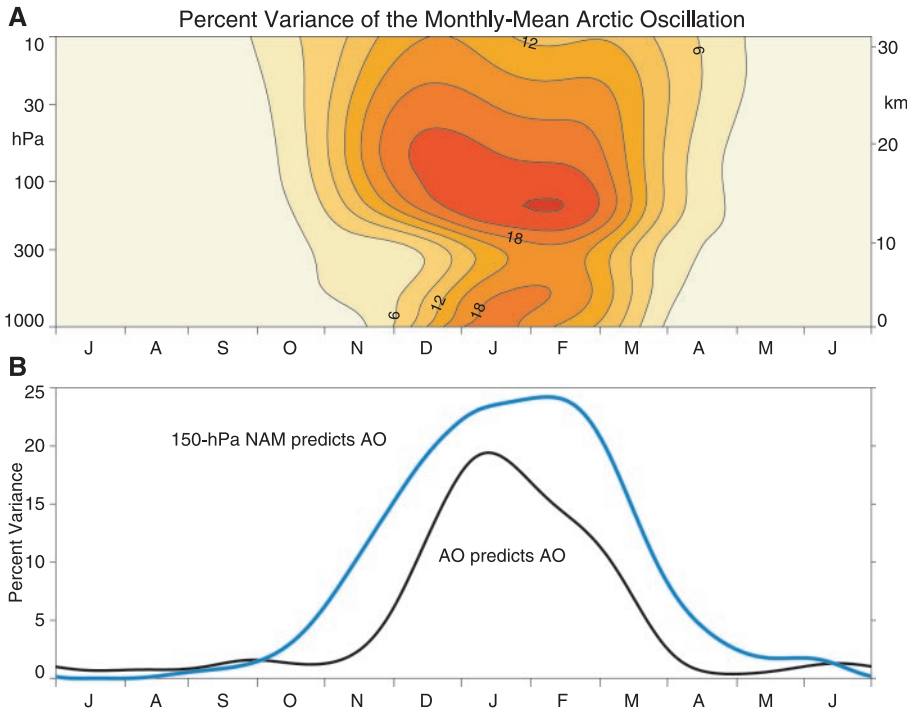

Fig. 2. (**A**) Predictability of the monthly-mean AO after a 10-day lead. Values are obtained by linear regression between the daily NAM time series and the monthly-mean AO beginning after 10 days and are displayed as percent variance of the monthly-mean AO. Daily values represent an average using Gaussian weighting with a FWHM of 60 days. (**B**) Cross sections through (A) at 1000 and 150 hPa. The 150-hPa NAM (blue curve) predicts the monthly-mean AO better than the AO itself (black curve) does.

from planetary waves 1 and 2 had a greater effect on the NAM, especially at positive lags (Fig. 4B); when waves 3 and higher were used (Fig. 4C), the effect was similar to that for all waves (Fig. 4A). These results provide evidence that both planetary-scale and synoptic-scale tropospheric waves are affected by stratospheric NAM anomalies.

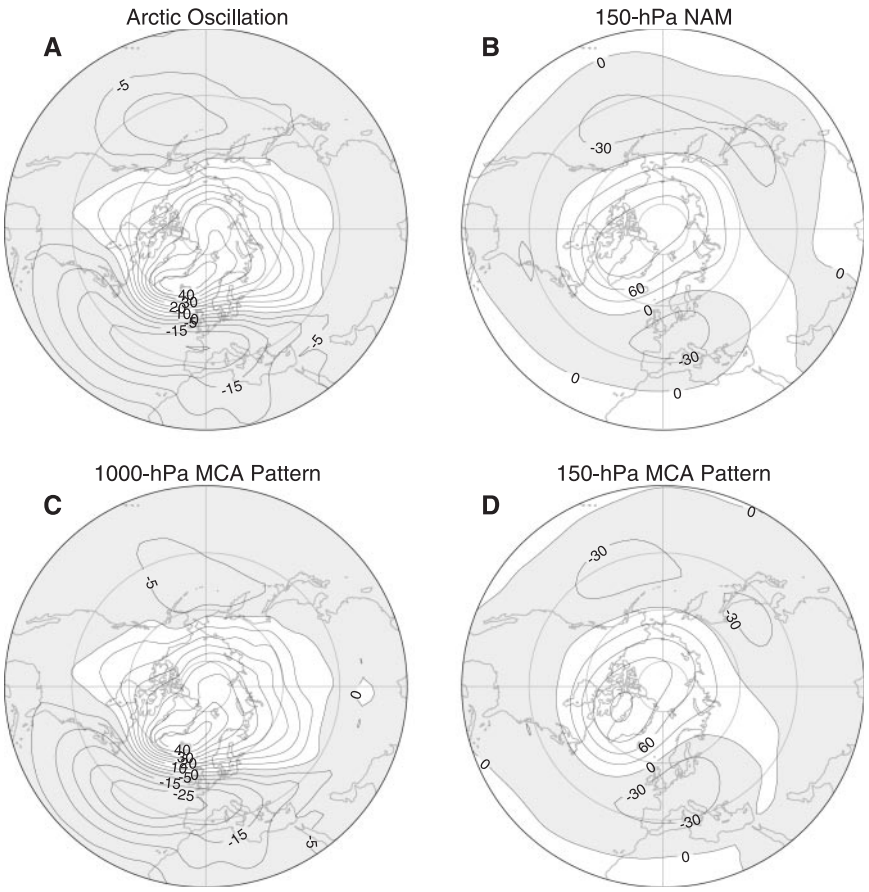

Fig. 3. (**A**) The AO regression pattern (in geopotential meters). (**B**) The 150-hPa NAM. (**C** and **D**) Leading MCA patterns between geopotential at 150 hPa and monthly-mean geopotential at 1000 hPa beginning after 10 days (centered 25 days later). For comparison with the EOF patterns, the data in (C) are normalized to have the same area-weighted spatial variance as in (A), and the data in (D) are normalized to have the same area-weighted spatial variance as in (B). The area-weighted spatial correlation is 0.96 between (A) and (C), and 0.96 between (B) and (D).

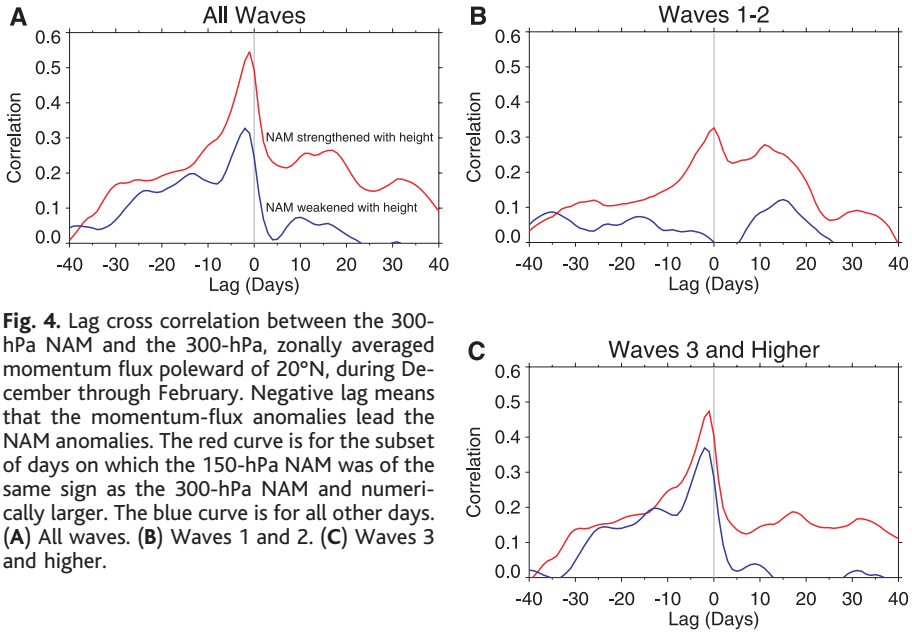

Fig. 4. Lag cross correlation between the 300-hPa NAM and the 300-hPa, zonally averaged momentum flux poleward of 20°N, during December through February. Negative lag means that the momentum-flux anomalies lead the NAM anomalies. The red curve is for the subset of days on which the 150-hPa NAM was of the same sign as the 300-hPa NAM and numerically larger. The blue curve is for all other days. (**A**) All waves. (**B**) Waves 1 and 2. (**C**) Waves 3 and higher.

Other mechanisms allow stratospheric processes to affect the troposphere, such as "downward control" (*37*), which relates steady-state wave drag to vertical mass flow (and by continuity, surface pressure changes), or planetary wave reflection (*38*, *39*). Our results are also consistent with studies of potential vorticity "inversion" in which lower stratospheric circulation anomalies induce AO-like changes to surface pressure of realistic magnitudes (*40*).

Our results have implications for numerical extended-range weather forecasting. Forecast models that do not adequately resolve the stratosphere (or that do not have realistic NAM anomalies in the lowermost stratosphere) will likely not be able to simulate the additional predictive skill from the stratospheric memory effect. A complete understanding of the details of the mechanism by which the lower stratospheric NAM affects waves in the upper troposphere will likely require carefully designed numerical experiments. On longer time scales, stratosphere-troposphere coupling would presumably allow stratospheric signals (e.g., greenhouse gas and ozone changes, solar-ultraviolet variations, and the quasi-biennial oscillation) to affect surface climate and trends in the stratospheric NAM to be reflected in the AO index.

References and Notes

1. J. G. Charney, J. Shukla, in *Proceedings of the Symposium on Monsoon Dynamics*, New Delhi, December 1977, J. Lighthill, R. P. Pearce, Eds. (Cambridge University Press, Cambridge, 1981), pp. 99–109.
2. World Meteorological Organization, *Manual on Global Data Processing Systems* (World Meteorological Organization, Geneva, 1992), vol. 1.
3. M. Kanamitsu *et al.*, *Bull. Am. Meteor. Soc.* **83,** 1019 (2002).
4. M. Hoerling, A. Kumar, *Science* **299,** 691 (2003).
5. R. A. Madden, P. R. Julian, *J. Atmos. Sci.* **28,** 702 (1971).
6. M. P. Baldwin, T. J. Dunkerton, *J. Geophys. Res.* **104,** 30937 (1999).
7. M. P. Baldwin, T. J. Dunkerton, *Science* **294,** 581 (2001).
8. D. W. J. Thompson, M. P. Baldwin, J. M. Wallace, *J. Climate* **15,** 1421 (2002).
9. D. W. J. Thompson, J. M. Wallace, *Geophys. Res. Lett.* **25,** 1297 (1998).
10. J. W. Hurrell, *Science* **269,** 676 (1995).
11. J. M. Wallace, *Q. J. R. Meteorol. Soc.* **126,** 791 (2000).
12. "Zonal" means in the east-west direction, with positive values for winds blowing from the west.
13. D. W. J. Thompson, J. M. Wallace, *Science* **293,** 85 (2001).
14. The NAM is defined as the leading empirical orthogonal function (EOF) of slowly varying (for instance, month-to-month), wintertime, hemispheric geopotential at each isobaric level and is the spatial pattern that accounts for the greatest fraction of geopotential variance. Daily indices of the annular modes are calculated for each level by projecting daily geopotential anomalies onto the leading EOF patterns. For details of the calculation, see (*7*).
15. During December through February, the daily correlation between the NAM at 10 hPa and the zonal-mean wind at 10 hPa, 60°N, is 0.96.
16. Wave-induced, angular-momentum transport, driven

by upward-propagating waves, leads to downward phase propagation of wind anomalies. The downward phase propagation creates what may be an illusion of downward influence, especially when the data are smoothed in time. Downward phase propagation does not in itself imply that anomalies at lower levels originate at upper levels. The stratosphere is modified by waves originating in the troposphere, altering the conditions for planetary-wave propagation in such a way as to draw mean-flow anomalies downward.
17. We used the National Centers for Environmental Prediction (NCEP) reanalysis data for 1000 to 10 hPa during 1958 to 2002 on a 2.5° longitude by 2.5° latitude grid. The NCEP reanalysis data were obtained from the National Oceanic and Atmospheric Administration–Cooperative Institute for Research in Environmental Sciences (NOAA-CIRES) Climate Diagnostics Center.
18. For the Southern Hemisphere, we used NCEP data from 1979 to 2001. Stratospheric data before 1979 are considered unreliable, and we did not use the highly unusual winter-spring events of 2002, which included the only observed major stratospheric warming in the Southern Hemisphere.
19. D. W. J. Thompson, J. M. Wallace, *J. Climate* **13**, 1000 (2000).
20. The stratospheric NAM variance peaks in midwinter (*6*).
21. W. A. Norton, *Geophys. Res. Lett.* **30**, 1627 (2003).
22. The question of causality, i.e., whether the stratosphere causes changes to the troposphere, is irrelevant for the forecasting problem.
23. A. J. Charlton, A. O'Neill, D. B. Stephenson, W. A. Lahoz, M. P. Baldwin, *Q. J. R. Meteorol. Soc.*, in press.
24. We use the square of the anomaly correlation to measure skill.
25. The AO accounts for 24% of the variance of monthly-mean 1000-hPa geopotential during December through February.
26. Artificial skill is an overestimate of the real skill of a forecasting system caused by the inclusion of the same data to evaluate the skill that was used to develop or train the forecasting system. Artificial skill can be avoided by the use of independent training and assessment data sets. Artificial skill often occurs in practice because of the presence of long-term trends in the data set (*42*).
27. Because it is persistent, the AO adds predictive skill on shorter time scales.
28. MCA is also known as singular value decomposition analysis (*41*).
29. T. G. Shepherd, *J. Meteorol. Soc. Japan* **80**, 769 (2002).
30. V. Limpasuvan, D. H. Hartmann, *J. Climate* **13**, 4414 (2000).
31. P. H. Haynes, T. G. Shepherd, *Q. J. R. Meteorol. Soc.* **115,** 1181 (1989).
32. During December through February, the daily correlation between 300-hPa momentum-flux anomalies (latitudinally averaged north of 20°N) and the rate of change of the AO index is 0.46.
33. D. Lorenz, D. Hartmann, *J. Climate*, **16**, 1212 (2003).
34. They found similar lag correlations between the leading EOF of 1000- to 100-hPa zonal wind and eddy momentum-flux convergences.
35. When the NAM strengthened with height, the mean was 0.028 and the standard deviation was 0.90. When the NAM weakened with height, the mean was −0.018 and the standard deviation was 1.06.
36. P. Chen, W. A. Robinson, *J. Atmos. Sci.* **49,** 2533 (1992).
37. P. H. Haynes, C. J. Marks, M. E. McIntyre, T. G. Shepherd, K. P. Shine, *J. Atmos. Sci.* **48**, 651 (1991).
38. J. Perlwitz, H.-F. Graf, *Geophys. Res. Lett.* **28,** 271 (2001).
39. J. Perlwitz, N. Harnik, *J. Climate*, in press.
40. R. X. Black, *J. Climate*, **15**, 268 (2002).
41. H. von Storch, F. W. Zwiers, *Statistical Analysis in Climate Research* (Cambridge Univ. Press, Cambridge, 1999), p. 321.
42. I. T. Jolliffe, D. B. Stephenson, Eds. *Forecast Verification: A Practitioner's Guide in Atmospheric Science* (Wiley, New York, 2003), p. 203.
43. We thank P. H. Haynes, D. A. Ortland, W. A. Robinson, S. Schubert, and T. G. Shepherd for discussions and A. Worsham for assistance with Fig. 1C. Supported by NSF's Climate Dynamics Program, NOAA's Office of Global Programs, NASA's Supporting Research and Technology Program for Geospace Sciences, NASA's Living With a Star Program, and NASA's Oceans, Ice, & Climate Program (M.P.B.); NSF's CAREER program (D.W.J.T.); and NOAA's Office of Global Programs (T.J.D.).

22 May 2003; accepted 3 July 2003

Role of Adaptor TRIF in the MyD88-Independent Toll-Like Receptor Signaling Pathway

Masahiro Yamamoto,[1] Shintaro Sato,[1,2] Hiroaki Hemmi,[1] Katsuaki Hoshino,[1,4] Tsuneyasu Kaisho,[1,4] Hideki Sanjo,[1] Osamu Takeuchi,[1] Masanaka Sugiyama,[1] Masaru Okabe,[3] Kiyoshi Takeda,[1,2] Shizuo Akira[1,2]*

Stimulation of Toll-like receptors (TLRs) triggers activation of a common MyD88-dependent signaling pathway as well as a MyD88-independent pathway that is unique to TLR3 and TLR4 signaling pathways leading to interferon (IFN)-β production. Here we disrupted the gene encoding a Toll/IL-1 receptor (TIR) domain-containing adaptor, TRIF. TRIF-deficient mice were defective in both TLR3- and TLR4-mediated expression of IFN-β and activation of IRF-3. Furthermore, inflammatory cytokine production in response to the TLR4 ligand, but not to other TLR ligands, was severely impaired in TRIF-deficient macrophages. Mice deficient in both MyD88 and TRIF showed complete loss of nuclear factor kappa B activation in response to TLR4 stimulation. These findings demonstrate that TRIF is essential for TLR3- and TLR4-mediated signaling pathways facilitating mammalian antiviral host defense.

TLRs recognize specific patterns of microbial components and are critical in provoking innate immune responses through activation of signaling cascades via Toll/IL-1 receptor (TIR) domain-containing adaptors, such as MyD88 and TIRAP (*1*, *2*). MyD88 is common to all the TLRs, whereas TIRAP is specifically involved in TLR2- and TLR4-mediated signaling pathways (*3*–*5*). In addition to the common MyD88-dependent pathway, TLR3 and TLR4 utilize a MyD88-independent signaling pathway that leads to the activation of IRF-3 and induction of IFN-β (*6*–*8*). TIR domain-containing adaptor inducing IFN-β (TRIF) was recently identified as a third adaptor and was shown to activate IFN-β expression via TLR3 (*9*, *10*).

To assess the physiological role of TRIF, we generated mice lacking the *Trif* gene [supporting online material (SOM) Text and fig. S1]). Mutant mice homozygous for the disrupted *Trif* allele were born at the expected mendelian ratio and grew to be healthy in specific-pathogen–free conditions.

Previous in vitro studies have suggested that TRIF is involved in production of IFN-β in response to double-stranded RNA and its analog poly(I:C), both of which are recognized by TLR3 (*9*–*11*). Therefore, we first analyzed poly(I:C)-induced messenger RNA (mRNA) expression of IFN-β and several IFN-inducible genes, such as RANTES, IP-10, and MCP-1, in peritoneal macrophages (Fig. 1A). Macrophages from TRIF$^{-/-}$ mice showed impaired expression of IFN-β and IFN-inducible genes in response to poly(I:C), which is consistent with results seen in TLR3$^{-/-}$ mice (*11*, *12*). In addition, splenocytes from TRIF$^{-/-}$ mice showed severely defective proliferation in response to poly(I:C), but not to the TLR9 ligand CpG DNA (Fig. 1B). TRIF$^{-/-}$ B cells were also severely impaired in poly(I:C)-induced, but not anti-IgM Ab (antibody to immunoglobulin M)–induced, augmentation of surface expression of CD69, CD86, and major histocompatibility complex (MHC) class II (Fig. 1C). Thus, TRIF$^{-/-}$ mice showed defective responses to poly(I:C), indicating that TRIF is essential for TLR3-mediated signaling pathways.

In addition to the TLR3 ligand, the TLR4 ligand LPS has been shown to induce IFN-β and subsequent expression of IFN-inducible genes in a MyD88-independent manner (*6*–*8*). We analyzed LPS-induced mRNA expression of IFN-inducible genes

[1]Department of Host Defense, Research Institute for Microbial Diseases, Osaka University, [2]ERATO, Japan Science and Technology Corporation, [3]Genome Information Research Center, 3-1 Yamada-oka, Suita Osaka 565-0871, Japan. [4]RIKEN Research Center for Allergy and Immunology, 1-7-22 Suehiro-cho, Tsurumiku, Yokohama, Kanagawa 230-0045, Japan

*To whom correspondence should be addressed. E-mail: sakira@biken.osaka-u.ac.jp